J. Appl. Comput. Mech., xx(x) (2026) 1-14
DOI: 10.22055/jacm.2025.48636.5383

ISSN: 2383-4536
jacm.scu.ac.ir

Shahid Chamran
University of Ahvaz

Journal of
Applied and Computational Mechanics

Research Paper

A Synergistic XFEM-RBF-MOPSO Based Approach for Multi-Crack Parameter Inversion

Guizhong Xie[1], Zhengyang Zhou[1], Hao Li[1], Hongfei Zhai[1], Chao Wu[1], Shenshen Chen[2], Jun Liu[3], Yang Liu[3], Jie Zhou[3]

[1] Henan Provincial Key Laboratory of Intelligent Manufacturing of Mechanical Equipment, Zhengzhou University of Light Industry, Zhengzhou, 450002, Henan, China, Email: midsunzhou@163.com (Z.Z.); Wuchao@zzuli.edu.cn (C.W.)

[2] School of Civil Engineering and Architecture, East China Jiaotong University, Nanchang, 330013, Jiangxi, China, Email: chenshenshen@tsinghua.org.cn

[3] State Key Laboratory of Mining Heavy Equipment, CITIC Heavy Industries Co., Ltd, Luoyang, 471039, Henan, China, Email: zhoujie20192024@163.com (J.Z.)

Received July 26 2025; Revised November 28 2025; Accepted for publication December 29 2025.
✉ Corresponding authors: Z. Zhou (midsunzhou@163.com); C. Wu (Wuchao@zzuli.edu.cn)
© 2026 Published by Shahid Chamran University of Ahvaz

Abstract. This paper proposes an integrated XFEM-RBF-MOPSO framework for the inversion of multiple crack parameters from displacement data. High-fidelity forward response samples are generated by the extended finite element method (XFEM) using optimal Latin hypercube sampling (OLHS). The XFEM results are used to construct a radial basis function (RBF) surrogate, which approximates the mapping between crack parameters and displacement responses. Multi-objective particle swarm optimization (MOPSO) is employed to search the parameter space using the RBF surrogate in order to match the observed displacements, thereby reducing the computational cost. This is because the RBF surrogate has higher predictive accuracy than the Kriging surrogate under limited-sample conditions, as verified by cross-validation. Our approach is validated through three numerical examples, including collinear double-edge cracks, two parallel internal cracks, and three parallel internal cracks. The crack-tip coordinates obtained by the combined MOPSO-RBF approach are in good agreement with those of the actual cases. The results demonstrate better convergence and computational efficiency, indicating that the proposed approach is a promising approach for practical multi-crack inversion.

Keywords: Crack inversion; Extended finite element method; Radial basis function; Multi-objective optimization; Particle swarm algorithm.

1. Introduction

Fatigue cracks are a major cause of failure in engineering structures such as bridges, aircraft, and pressure vessels. Therefore, accurately identifying the location and size of cracks in engineering structures is crucial for ensuring structural reliability. Existing approaches for crack identification can be broadly categorized into three types: physics-based numerical identification methods, image-processing-based or machine-learning- and deep-learning-based identification methods, and surrogate-model-based numerical identification methods.

In the field of crack identification, physics-based numerical inversion methods were among the earliest approaches applied. In these methods, numerical techniques such as the finite element method (FEM), extended finite element method (XFEM), or boundary element method (BEM) are employed for forward analysis to obtain structural displacement, strain, and other responses. Global optimization algorithms are combined with these numerical methods to invert crack parameters, including crack location and size. Early research on numerical inversion methods mainly focused on the integration of XFEM with optimization algorithms.

Rabinovich et al. proposed an inversion framework combining XFEM and the Genetic Algorithm (GA), capable of effectively locating cracks without remeshing and significantly improving dynamic identification accuracy [1, 2]. Zhang et al. and Khatir et al. developed crack identification methods based on XFEM or FEM models using structural vibration frequencies as features, obtaining the crack location and depth in experimental beam structures using particle swarm optimization (PSO). However, these methods are sensitive to shallow cracks and noise [3, 4]. Bouhala et al. combined XFEM with a cohesive zone model for fracture parameter identification in composites, demonstrating the importance of physics-based modeling for inversion accuracy [5]. Agathos et al. proposed a stabilized XFEM coupled with multiscale global optimization, which was applied to three-dimensional multiple cracks in complex structures [6]. Feerick et al. applied XFEM to simulate crack propagation in anisotropic cortical bone, verifying the effectiveness of this method in predicting crack behavior [7]. Gao et al. and Dai et al. integrated XFEM with high-order hybridization operators or improved inverse XFEM for crack identification in tunnels and large-scale structures, thereby enhancing numerical stability and engineering applicability [8, 9].

Published online: January 03 2026

Beyond mechanical responses, some researchers have also employed parameters from other physical fields to invert for crack location and size. For instance, electric potential field inversion methods based on BEM have been developed, in which electric potential tomography was used for non-destructive measurement of three-dimensional hidden cracks [10]. Noii et al. combined phase-field modeling with Bayesian inversion to identify fracture parameters in ductile materials, highlighting the potential of integrating physical consistency with probabilistic inversion frameworks [11].

Overall, physics-based numerical inversion methods offer strong physical interpretability and generality. However, these methods are sensitive to measurement noise and have a high computational cost, making them difficult to extend to multi-crack or high-dimensional problems. Thus, surrogate model–based and data-driven methods for crack identification are becoming increasingly common due to their computational efficiency and robustness.

In recent years, with the rapid development of computer vision and artificial intelligence technologies, image-based crack detection methods have become an active research area. These methods acquire high-resolution images of structural surfaces and automatically identify the presence and morphological features of cracks using image processing or machine learning and deep learning models, enabling rapid assessment of surface damage. Traditional image processing approaches rely on algorithms such as filtering, edge detection, and morphological analysis to identify cracks, whereas machine-learning-based techniques train models on large-scale datasets for pixel-level crack segmentation and classification.

Relevant literature [12] shows that image-recognition-based methods have achieved significant improvements in detection accuracy and automation, making them suitable for the rapid non-destructive inspection of surface cracks in bridges, roads, tunnels, and similar infrastructure. However, these methods struggle to capture internal cracks and three-dimensional crack parameters.

Overall, physics-based numerical inversion methods suffer from high computational costs and low convergence efficiency. Although image-processing-based and machine-learning- and deep-learning based approaches are highly efficient, they struggle to capture the internal geometric and mechanical characteristics of cracks. To address this issue, researchers have proposed surrogate-model–based crack identification techniques. These methods construct an approximate model for crack identification using a limited number of samples, which replace forward analyses based on FEM or XFEM and enable rapid prediction or inversion of crack parameters. Depending on whether optimization algorithms are incorporated, these methods can be broadly categorized into two types: direct surrogate identification methods and surrogate-plus-optimization inversion methods.

Direct surrogate identification methods utilize surrogate models to establish a functional mapping between structural response and crack characteristics, thereby enabling the prediction of crack location or damage state. Corrado et al. proposed a crack localization method for beam structures using Gaussian process regression, capable of simultaneously identifying single and multiple crack locations and quantifying prediction uncertainty [13]. Liu et al. implemented crack identification for composite sandwich structures based on Gaussian process classification, transforming the crack detection problem into a probabilistic classification problem [14]. Wang et al. proposed an online crack assessment method using a heteroscedastic Gaussian process model, improving the modeling accuracy of noise and uncertainty in traditional Gaussian process models [15]. Zhong et al. combined XFEM data with a neural network surrogate model to achieve high-accuracy identification of multi-crack structures, demonstrating the superiority of deep surrogate models under complex geometric conditions [16]. In comparison, direct surrogate methods are computationally efficient and structurally simple, but their accuracy depends on the quality of sample distribution and lack generalization capability in high-dimensional parameter inversion.

Surrogate-plus-optimization inversion methods are based on surrogate models and intelligent optimization algorithms, such as PSO and GA, to search for crack parameters that minimize the error between predicted responses and observed data, thereby achieving accurate inversion and identification. Gao et al. proposed a crack identification framework based on the Kriging model, using FEM simulations to generate sample data and establishing an approximate relationship between crack parameters and structural responses, thereby inverting crack location and depth through error minimization [17]. Gao et al. further extended this method to cantilever plate structures, verifying its accuracy and applicability in two-dimensional crack identification [18]. Wang et al. combined the Kriging model with the improved nondominated sorting genetic algorithm-III (NSGA-III) to achieve crack parameter inversion in rotating machinery systems, significantly improving computational efficiency and identification accuracy [19]. These methods reduce iterative costs while maintaining numerical accuracy, and represent one of the most widely used inversion strategies in engineering crack identification.

Surrogate-model-based crack identification methods, which combine numerical stability and computational efficiency, have become an important research direction bridging physics-based inversion and data-driven approaches. Direct surrogate methods are suitable for rapid localization and online monitoring, whereas surrogate-plus-optimization based inversion methods inversion methods are more appropriate for precise identification and multi-parameter inversion. In the process of identifying crack location and size in engineering structures, interactions among multiple cracks are often involved, which can significantly alter the crack-tip stress field and energy release characteristics [20]. Therefore, the coupling effects among multiple cracks must be considered in crack identification to avoid errors arising from the single-crack assumption. Based on this, this paper proposes a high-accuracy multi-crack identification method for thin plate structures, integrating XFEM, surrogate models, and optimization algorithms to achieve accurate inversion and localization.

The remainder of this paper is organized as follows. Section 2 presents the theoretical framework of the proposed XFEM-RBF-MOPSO method for multi-crack inversion. Section 3 validates the proposed approach through numerical case studies and evaluates the accuracy of the inversion results. Finally, Section 4 presents the main conclusions of this study.

2. Proposed XFEM-RBF-MOPSO Framework for Multi-Crack Inversion

2.1. Extended finite element method

XFEM enriches the standard finite element approximation with additional functions that capture discontinuities and singularities without remeshing. Specifically, a Heaviside function models displacement jumps across cracks, while asymptotic crack-tip functions capture stress singularities. This enables accurate representation of crack initiation and propagation within a fixed mesh [21-23].

The displacement field can be expressed as [24]:

$$\mathbf{u}(\mathbf{x}) = \sum_{i\in I} N_i(\mathbf{x})\mathbf{u}_i + \sum_{j\in J} N_j(\mathbf{x})H(\mathbf{x})\mathbf{a}_j + \sum_{k\in K} N_k(\mathbf{x})\sum_{\alpha=1}^{4} F_\alpha(\mathbf{x})\mathbf{b}_k^\alpha \tag{1}$$

where $\boldsymbol{u}(\mathbf{x})$ is the displacement vector at position x; $N_i(\mathbf{x})$ is the standard finite-element shape function of node i; $\mathbf{u}_i$ is the conventional nodal displacement; $H(\mathbf{x})$ is the Heaviside function representing the displacement jump across the crack surface; $\mathbf{a}_j$ denotes the additional degrees of freedom of the nodes j in the set J enriched by $H(x)$; $F_\alpha(\mathbf{x})$ (α = 1,…,4) are the crack-tip asymptotic enrichment functions [25-27]; $\mathbf{b}_k^{\alpha}$ are the corresponding enriched nodal degrees of freedom for nodes k in the set K; and I, J, and K represent the collections of standard, Heaviside-enriched, and crack-tip-enriched nodes, respectively.

Based on this displacement approximation, applying the standard finite element derivation process ultimately yields a system of linear algebraic equations describing the equilibrium of the system:

$$K^{XFEM}\mathbf{U}^{XFEM} = \mathbf{F}^{XFEM} \tag{2}$$

The global degree of freedom vector $\mathbf{U}^{XFEM}$ contains both the standard degrees of freedom of all nodes and the enriched degrees of freedom of the enriched nodes, denoted as $\{u,b,c\}^T$. The global stiffness matrix K^{XFEM} and the load vector $\mathbf{F}^{XFEM}$ incorporate contributions from standard, enriched, and coupling terms [28]. Their computation requires specialized numerical integration methods to handle discontinuities and singularities within elements. Solving this system yields the full-field response of the cracked structure. The core advantage of XFEM lies in its flexibility and efficiency in handling discontinuity problems, particularly due to its ability to avoid mesh reconstruction during crack propagation simulations [29, 30]. Crack geometry is described by a level set method [31], in which the signed distance functions define crack surfaces and tips [32, 33]. This allows flexible insertion of single or multiple cracks without altering the mesh topology.

In this study, XFEM is served as a high-fidelity forward model to generate displacement responses under given crack configurations. These responses form the training dataset for the surrogate model described in Section 2.2.

2.2. RBF surrogate model

In inversion problems such as crack identification, high-fidelity models with XFEM establish the link between physical inputs (crack parameters) and outputs (displacement). However, since inversion requires repeated evaluations of the forward model during optimization, directly using XFEM would be computationally impractical. A surrogate model, trained on selected sample points, approximates the XFEM response and replaces it in optimization algorithms like multi-objective particle swarm optimization (MOPSO). This significantly reduces computational time while preserving acceptable accuracy.

We choose the RBF network over alternatives such as Kriging because it is a universal approximator that can be trained efficiently through linear least squares, while also showing robust performance when only a limited number of samples are available, which is consistent with our optimal Latin hypercube sampling (OLHS) dataset. In addition, the radial locality of RBF makes them particularly suitable for modeling displacement fields that are smooth but spatially varying. To further demonstrate this advantage, a subsequent section presents a direct comparison of RBF and Kriging using the same training sample size, including both surrogate-model accuracy and the final crack-inversion results.

The core of the RBF neural network is based on the theory of radial basis functions, where the response of a network node depends on the distance between the input vector and the center vector associated with that node [34]. A typical RBF network consists of three layers [35,36]:

The input layer receives external input data. The input vector $\mathbf{p} \in R_d$ represents the d-dimensional geometric parameters describing the multi-crack state. The nodes in the input layer simply transmit p to the next layer.

The hidden layer is the key layer for achieving nonlinear mapping. It consists of N RBF neurons, where each neuron i has a center vector $\mathbf{c}_i \in R_d$ and an activation function, which is a radially symmetric RBF φ. The most used RBF is the Gaussian function:

$$\varphi_i(\mathbf{p}) = \varphi(\|\mathbf{p}-\mathbf{c}_i\|) = \exp\left(-\frac{\|\mathbf{p}-\mathbf{c}_i\|^2}{2\sigma_i^2}\right) \tag{3}$$

where $\mathbf{p} \in R_d$ denotes the input vector, $\mathbf{c}_i$ is the center of the i-th neuron, $\sigma_i > 0$ is its width parameter, and $\| \mathbf{p} - \mathbf{c}_i \|$ represents the Euclidean distance between $\mathbf{p}$ and $\mathbf{c}_i$. The width σ_i governs the effective receptive field of the i-th neuron. Mapping the input space into an N-dimensional feature space, the hidden layer enables the network to approximate complex nonlinear relationships. The center vectors $\mathbf{c}_i$ and width parameters σ_i therefore constitute key structural parameters of the RBF network.

The output layer is composed of m linear neurons. It generates the final output of the network. In this study, the output vector $\hat{\mathbf{u}}_k \in R^m$ represents the predicted m-dimensional structural displacement response corresponding to the input crack parameters $\mathbf{p}$. The k-th output $\hat{\mathbf{u}}_k$ is the weighted sum of the outputs from all neurons in the hidden layer:

$$\hat{\mathbf{u}}_k = \sum_{i=1}^{N} w_{ik}\varphi_i(\mathbf{p}) = \sum_{i=1}^{N} w_{ik}\exp\left(-\frac{\| \mathbf{p}-\mathbf{c}_i\|^2}{2\sigma_i^2}\right) \tag{4}$$

where w_{ik} is the weight connecting the i-th hidden neuron to the k-th output neuron.

When using the RBF network as a surrogate model, a dataset $S = \{(\mathbf{p}_j, \mathbf{u}_j)\}_{j=1}^{M}$ containing M samples is first generated by running the high-precision XFEM model, where $\mathbf{p}_j$ represents the input crack parameters, and $\mathbf{u}_j$ is the corresponding displacement calculated by XFEM. The RBF network is trained using this dataset. The objective is to minimize the error between the surrogate model predicted output $\hat{\mathbf{u}}_j$ and the true XFEM output $\mathbf{u}_j$, improving the accuracy of the surrogate model.

2.3. MOPSO optimization algorithm

After constructing the surrogate model, the next step is to perform efficient inversion calculations using it. The inversion of crack parameters is essentially an optimization problem, in which an optimal set of crack parameters $\mathbf{p}$ is obtained by minimizing the difference between the predicted displacement response $\hat{\mathbf{u}}$ of the surrogate model and measured displacement response $\mathbf{u}_{obs}$.

In the numerical examples presented in this study, the parameter vector to be identified is:

$$Q = \{x_1, y_1, x_2, y_2, \ldots\}, \tag{5}$$

where x_1, y_1, x_2, y_2, … denote the coordinate positions of the crack tips.

The objective function is:

$$O(Q) = \sum \frac{\hat{\mathbf{u}} - \mathbf{u}_{obs}}{\hat{\mathbf{u}}} \tag{6}$$

Considering the potential presence of multiple optimization objectives in practical problems, this study adopts MOPSO to find the crack coordinates that minimize O(Q), thereby inverting the initial crack coordinates.

The standard PSO algorithm simulates the social behavior observed in swarms. The algorithm maintains a swarm of N_p particles (candidate solutions). Each particle i has a position vector $\mathbf{p}_i \in R^d$ and a velocity vector $\mathbf{v}_i \in R^d$. At each iteration t, the velocity and position of the particles are updated according to the following equations:

$$\mathbf{v}_i(t+1) = w\mathbf{v}_i(t) + c_1 r_1\left(pbest_i(t) - \mathbf{p}_i(t)\right) + c_2 r_2\left(gbest(t) - \mathbf{p}_i(t)\right) \tag{7}$$

where w is the inertia weight, adjusting the influence of the previous velocity on the current velocity. c_1, c_2 are learning factors (or acceleration constants), which adjust the weights for learning from the individual best and global best, respectively. r_1, r_2 are random numbers uniformly distributed in the interval [0, 1]. $pbest_i(t)$ is the personal best position found by particle i up to iteration t. $gbest_i(t)$ is the global best position found by the entire population up to iteration t.

Position update:

$$\mathbf{p}_i(t+1) = \mathbf{p}_i + \mathbf{v}_i(t+1) \tag{8}$$

MOPSO is an extension of the standard PSO algorithm to the field of multi-objective optimization. MOPSO uses a *pbest* update rule based on Pareto dominance and selects a leader g_i from a dynamically maintained archive of non-dominated solutions, driving the particle swarm to converge to the true Pareto front while exploring different regions along the front. This aligns well with the inherent requirements of multi-objective optimization problems, making it a powerful tool for solving such problems [37].

2.4. Overall inversion workflow

OLHS enhances Latin Hypercube Sampling (LHS) by introducing an optimization criterion-maximizing the minimum distance between sample points or minimizing correlations among sample points) [38,39]. This further refines the LHS design, resulting in a set of sample points that not only preserve uniformity of projections in each dimension, but also achieve enhanced space-filling and uniformity throughout the high-dimensional space [40].

To invert for the positions of multiple cracks efficiently and accurately, this paper proposes an integrated computational framework. To mitigate the high computational cost associated with XFEM-based parameter analysis, OLHS is used to generate N representative sample points in the multi-dimensional crack parameter space. The corresponding displacement responses can be obtained by simulating with the XFEM program developed in MATLAB at these sample points, forming a database that captures the crack parameter-displacement mapping. This database is then used to train an RBF neural network surrogate model. The trained RBF network can rapidly predict displacements, effectively replacing XFEM calculations during the inversion process [41].

Subsequently, the inversion task is formulated as an optimization problem to identify the crack parameters that minimize the discrepancy between the RBF-predicted and the target displacement. Given the complex solution landscape and potential multi-objective nature of the problem, MOPSO is employed to perform the optimization. MOPSO iteratively evaluates candidate crack parameters by querying the RBF surrogate model, conducting global searches, and converging to a Pareto-optimal solution set. This set yields high-quality candidate solutions that balance competing objectives in multi-crack inversion.

To illustrate the physical application of the proposed framework, the schematic configuration of the considered engineering system is presented in Fig. 1. This model represents a typical structural component (e.g., a plate section within a pressure vessel subjected to remote tensile stress). The system is characterized by multiple internal cracks, whose tip coordinates constitute the unknown parameters to be identified. The distinct markers (blue dots) distributed along the boundaries indicate the responding points where displacement responses are monitored. These observed data serve as the physical ground truth that drives the XFEM-RBF-MOPSO workflow to iteratively search for the accurate crack parameters.

3. Numerical Examples and Result Analysis

3.1. Collinear double-edge cracks under uniaxial tension

(1) Arrangement Scheme

Consider a rectangular plate of size 2 m×2 m with an elastic modulus E = 22000 Pa and Poisson's ratio ν = 0.33. The upper and lower edges of the plate are subjected to a uniform tensile stress σ = 1 MPa. In this example, the plate contains two horizontal edge cracks, each with a length of a = 0.4 m. The first crack extends horizontally to the right from the midpoint of the left boundary (0, 0), with the crack tip located at the true coordinate (0.4, 0). The second crack extends horizontally to the left from the midpoint of the right boundary (2.0, 0), with the crack tip located at the true coordinate (1.6, 0), as shown in Fig. 2. The plate is discretized using a structured mesh with n_H = 50 elements along the vertical direction, resulting in a total of 50×50 elements. Each element is a four-node quadrilateral, allowing for an accurate representation of the geometry and boundary conditions.

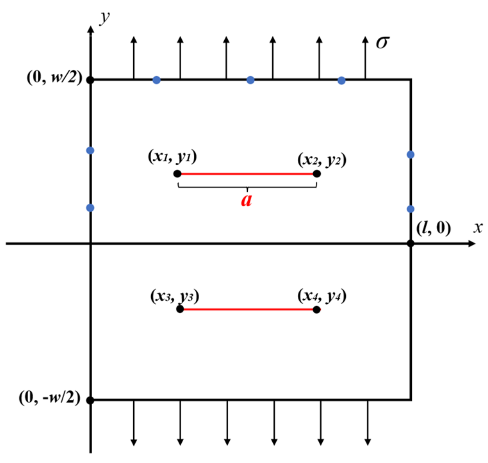

Fig. 1. Schematic configuration of the cracked plate model.

Table 1. Response point coordinates of the crack model.

Axis	1	2	3	4	5	6	7	8	9	10	11	12
X	0	0	0	0	0.4	0.8	1.2	1.6	2	2	2	2
Y	0.2	0.4	0.6	0.8	1	1	1	1	0.8	0.6	0.4	0.2

Table 2. Target displacement data.

x_1	y_1	x_2	y_2	U01	…	U12
0.4	0	1.6	0	0.000120014716231		0.000120851305837

Table 3. Sample data obtained from XFEM calculations (Unit: meter).

Number	x_1	y_1	x_2	y_2	U01	…	U12
1	0.4343	0.0263	1.497	-0.0465	0.0001823		0.0001482
2	0.3899	0.2	1.6828	-0.0788	0.0001523		0.0001028
3	0.2889	-0.1232	1.5535	-0.0505	0.0001151		0.0001653
…							
100	0.2889	-0.1636	1.7475	-0.002	0.00011544		0.0000970

Table 4. Numerical model configuration and parameters.

Item	Description
Geometry	2 m×2 m square plate
Material properties	Elastic modulus E = 22,000 Pa, Poisson's ratio ν = 0.33
Loading condition	Uniform tensile stress σ = 1MPa applied on top and bottom edges
Crack configuration	Two horizontal edge cracks: Crack 1: from (0, 0) to (0.4, 0) Crack 2: from (2.0, 0) to (1.6, 0)
Number of unknown parameters	4 (coordinates of 2 crack tips: $x_{1\text{-}2}$, $y_{1\text{-}2}$)
Parameter bounds	$x_1 \in [0.2, 0.6]$, $y_1 \in [-0.2, 0.2]$ $x_2 \in [1.4, 1.8]$, $y_2 \in [-0.2, 0.2]$
FE mesh	50 × 50 structured quadrilateral elements
Response points	12 points
OLHS sample size	100
Reference crack length a_0	0.4 m

(2) Surrogate Model Construction

To construct the training database required for the RBF surrogate model, the inverse parameter space of the crack tip coordinates was first defined. For collinear bilateral cracks, since the crack mouths are located at the structural edges with fixed positions, the unknown parameters to be inverted are specifically the crack tip coordinates of the two cracks. Specifically, the coordinate range of crack tip 1, (x_1, y_1), is set as $x_1 \in [0.2, 0.6]$, $y_1 \in [-0.2, 0.2]$. The coordinate range of crack tip 2, (x_2, y_2), is defined as $x_2 \in [1.4, 1.8]$, $y_2 \in [-0.2, 0.2]$. 100 sample points with good spatial coverage were selected in this four-dimensional parameter space using the OLHS method.

In the simulation, twelve response points were used to extract displacement data, with their exact coordinates listed in Table 1 and their locations on the plate indicated by the blue markers in Fig. 2. To enhance the representativeness of the surrogate model inputs, these points were concentrated in regions with significant displacement, mainly the upper half of the plate in this case [42]. The target displacement data for inversion were obtained by performing an XFEM simulation of the numerical model, where the crack coordinates were set according to the actual crack configuration described above, and extracting the displacements at the same twelve response points. The resulting values are listed in Table 2.

For these 100 sets of crack parameter combinations, high-precision XFEM forward simulations were performed for each set, and the displacement data at the predefined response points were collected, thereby forming a sample database containing $\{(x_1,y_1,x_2,y_2)_i,u_i\}_{i=1}^{100}$. The resulting samples from the XFEM calculations are presented in Table 3 and were subsequently used to train the RBF surrogate model. Numerical model configuration and parameters are presented in Table 4.

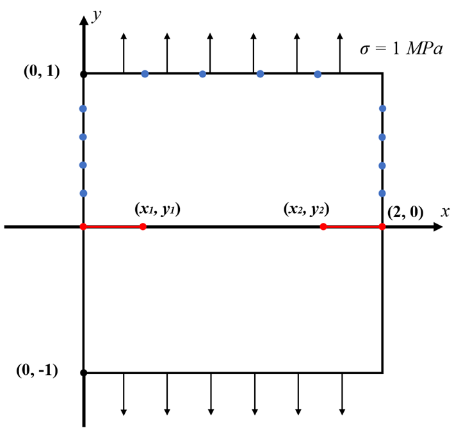

Fig. 2. Arrangement scheme.

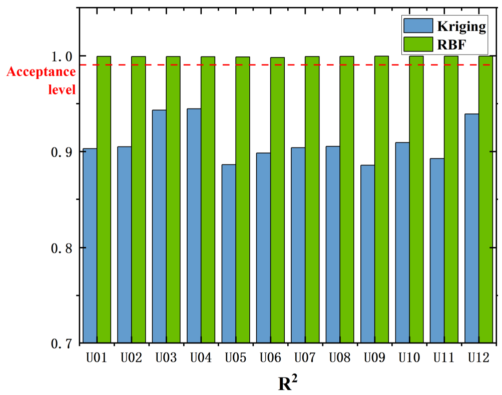

Fig. 3. Bar chart of R^2.

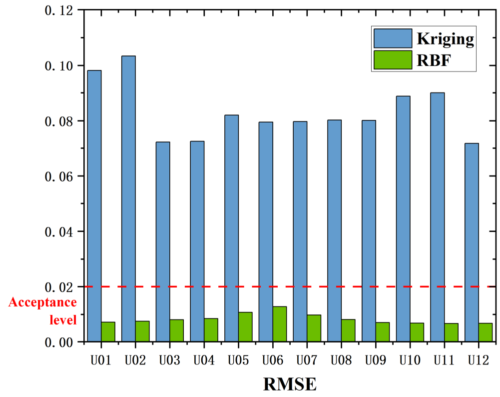

Fig. 4. Bar chart of RMSE.

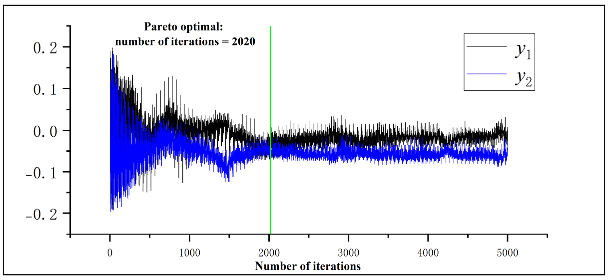

Fig. 5. Convergence history of y_1 and y_2.

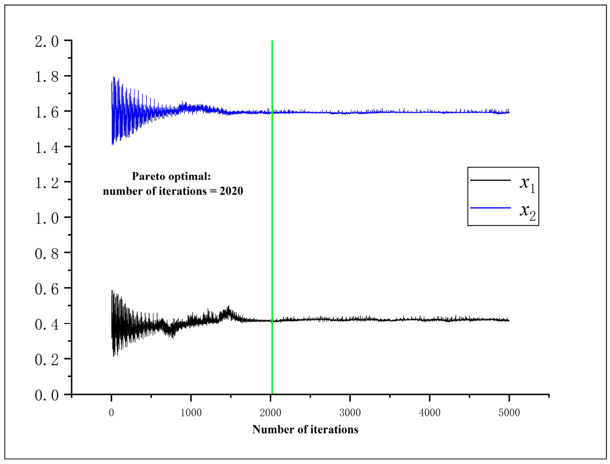

Fig. 6. Convergence history of x_1 and x_2.

(3) Accuracy Verification

To ensure the accuracy and reliability of the RBF surrogate model, this section presents the validation of the proposed method. Cross-validation was employed for evaluation. Specifically, out of the 100 sample points generated by OLHS and XFEM simulations, 20 points were randomly selected for cross-validation analysis. To quantitatively assess the predictive performance of the surrogate models, the coefficient of determination, R^2, and the root mean square error, RMSE, were used as key evaluation metrics. R^2 measures the proportion of variance in the data explained by the model (ideal value = 1), while RMSE represents the average magnitude of prediction errors (a smaller value indicates better performance). In this study, the acceptable thresholds were specified as $R^2 \geq 0.99$ and RMSE ≤ 0.02. The R^2 and RMSE values at the 12 response points (U01–U12), obtained through cross-validation, are presented in Figures 3 and 4 to compare the predictive accuracy of the RBF surrogate model with that of the Kriging model under the same training-sample size.

Figures 3 and 4 show that, with the same training sample size, the RBF surrogate consistently outperforms Kriging. Its R^2 values stay near 1.0 and above the 0.99 acceptance level, while its RMSE remains below 0.01 and well under the 0.02 threshold, whereas Kriging fails to meet these accuracy criteria across all response points.

The comprehensive evaluation results from cross-validation of R^2 and RMSE demonstrate that the trained RBF surrogate model possesses excellent predictive accuracy. This confirms that the RBF surrogate model has achieved sufficient accuracy to reliably emulate XFEM behavior and can be confidently used in the subsequent multi-crack inversion optimization process performed via MOPSO.

(4) Optimization Process and Results

After training the RBF surrogate model based on the generated sample database, the MOPSO algorithm was applied to solve the inversion problem. The objective function was formulated to minimize the error between the displacements predicted by the RBF surrogate model and the target displacements.

The MOPSO parameters were determined through a brief pilot study aimed at balancing convergence speed, exploration, and computational cost. A moderate swarm size-maintained population diversity without excessive forward evaluations; the inertia weight was gradually reduced to shift from global search to local refinement; and the cognitive and social coefficients were set to stabilize the interplay between individual and collective learning. The maximum particle velocity was scaled according to the admissible ranges of crack coordinates and radii, avoiding overshooting while maintaining efficient movement in the design space. These calibrated settings were then fixed for subsequent analyses, and the following two examples adopted the same parameter-selection rationale. The specific parameter settings of the MOPSO algorithm are shown in Table 5.

Table 5. MOPSO parameter settings.

Parameter	Maximum Iterations	Swarm Size	Inertia Weight	Global Increment	Particle Increment	Maximum Velocity
Value	100	50	0.1	0.3	0.5	0.1

Table 6. Inversion results.

Crack coordinates	(x_{inv}, y_{inv})	(x_{true}, y_{true})	E_{pos}(%)
(x_1, y_1)	(0.4157, 0.000547)	(0.4, 0)	3.96
(x_2, y_2)	(1.5922, -0.028693)	(1.6, 0)	7.43

Table 7. Comparison of E_{pos} values obtained from different approaches.

Crack coordinates	$E_{KR+MOPSO}$(%)	$E_{KR+NSGA}$(%)	$E_{RBF+MOPSO}$(%)
(x_1, y_1)	46.34	48.07	3.96
(x_2, y_2)	36.51	27.33	7.43

Table 8. Response point coordinates for the edge crack model.

Axis	1	2	3	4	5	6	7	8	9	10	11	12
X	0	0	0	0	0	0	2	2	2	2	2	2
Y	-2	-1	0	1	2	3	3	2	1	0	-1	-2

As shown in Figs. 5 and 6, the particle swarm initially explores widely within the defined parameter space, then quickly converges toward the optimal region, and finally stabilizes near specific values, demonstrating good convergence performance.

The MOPSO algorithm searches for a set of non-dominated solutions representing optimal trade-offs among multiple objectives. One representative Pareto-optimal solution is selected as the final inversion result. The Pareto-optimal solutions were obtained at iteration 2020.

To quantify the overall positional discrepancy between the inverted and true crack-tip coordinates, a normalized Euclidean distance is adopted. Let (x_{inv}, y_{inv}) and (x_{true}, y_{true}) denote the inverted and true crack-tip coordinates, respectively.

The positional error is defined as:

$$E_{pos} = \frac{\sqrt{\left(x_{inv} - x_{true}\right)^2 + \left(y_{inv} - y_{true}\right)^2}}{a_0} \times 100\% \tag{9}$$

where a_0 is the true length of the target crack used as the reference length.

Inversion results and error analysis is presented in Table 6. In this study, KR+MOPSO and KR+NSGA were adopted as benchmark methods, where KR denotes the Kriging surrogate model; MOPSO denotes the multi-objective particle swarm optimization algorithm and NSGA denotes the non-dominated sorting genetic algorithm, respectively. These combinations were selected based on established literature [17–19], which demonstrated the broad use of Kriging-based optimization frameworks in crack identification. To ensure methodological consistency, the surrogate model (Kriging) was fixed while the optimization algorithm varied, allowing a systematic comparison of optimization strategies.

This design highlights the superior performance of the proposed RBF surrogate under limited-sample conditions. For rigorous validation, additional MOPSO- and NSGA-based inversions were performed using Kriging surrogates trained with the same sample size as in the proposed method. The resulting crack-tip errors $E_{KR+MOPSO}$, $E_{KR+NSGA}$, and $E_{RBF+MOPSO}$ are compared in Tables 7, 14, and 21 across all numerical examples. This benchmarking framework ensures fair comparison under consistent sampling conditions and quantitatively confirms the enhanced accuracy and robustness of the XFEM-RBF-MOPSO approach for multi-crack parameter inversion.

As shown in Table 7, the RBF+MOPSO approach yields more accurate and stable predictions than the KR+MOPSO and KR+NSGA approaches under limited sample conditions.

3.2. Two parallel cracks under uniaxial tension

(1) Arrangement Scheme

Consider a rectangular plate with dimensions of 2 m×30 m, with an elastic modulus of E = 22000 Pa and a Poisson's ratio of ν = 0.33. The top and bottom edges of the plate are subjected to a uniform tensile stress of σ = 1 MPa. In this example, the plate contains two horizontal parallel internal cracks, each with a length of a = 1 m. The first crack is horizontally aligned, with the true coordinates of its two crack tips being (0.5, 1.0) and (1.5, 1.0). The second crack is also horizontally aligned, parallel to the first crack, and symmetric about the y = 0 axis (the transverse centerline of the plate), with the true coordinates of its two crack tips being (0.5, -1.0) and (1.5, -1.0), as shown in Fig. 8. The plate is discretized using a structured mesh with n_H = 400 elements along the vertical direction, resulting in a total of 6000×400 elements. Each element is a four-node quadrilateral, allowing for an accurate representation of the geometry and boundary conditions.

(2) Surrogate Model Construction

The inversion parameter space consists of the coordinates of the four crack tips of the two horizontal cracks, totaling eight inversion parameters. Denote the left and right crack tip coordinates of the upper crack as (x_1, y_1) and (x_2, y_2), and those of the lower crack as (x_3, y_3) and (x_4, y_4).

To generate the sample points required for RBF training using OLHS, the parameter ranges are defined as follows:

Upper Crack: $x_1 \in [0.25,0.75]$, $y_1 \in [0.75, 1.25]$, $x_2 \in [1.25,1.75]$, $y_2 \in [0.75, 1.25]$

Lower Crack: $x_3 \in [0.25,0.75]$, $y_3 \in [-1.25, -0.75]$, $x_4 \in [1.25,1.75]$, $y_4 \in [-1.25, -0.75]$

Subsequently, the OLHS method was applied within this eight-dimensional parameter space to generate a total of 500 sample points for the XFEM computations. Twelve response points were used to extract displacement data. Their exact coordinates are listed in Table 8, and their locations on the plate are indicated by the blue markers in Fig. 8.

Following the same procedures as in Section 3.1, the sample data obtained from the XFEM calculations are presented in Table 9, and the target displacement values are listed in Table 10. Numerical model configuration and parameters are presented in Table 11.

(3) Accuracy Verification

From the total of 500 sample points generated through OLHS and XFEM, 80 points were randomly selected for cross-validation analysis. The acceptable threshold for R^2 was set to 0.99, and for RMSE, to 0.025. The R^2 and RMSE values for the 12 response points (U01-U12), obtained through cross-validation, are presented in Figs. 9 and 10 to compare the predictive accuracy of the RBF surrogate with the Kriging model using the same training-sample size.

Table 9. Sample data obtained from XFEM calculations (Unit: meter).

	x_1	y_1	…	U01	…	U12
1	0.27	1.0175		0.000592984		0.000593639
2	0.6789	0.7961		0.000597680		0.000598827
3	0.4795	1.0486		0.000596282		0.000596742
500	0.7089	1.1909		0.000594180		0.000594852

Table 10. Target displacement data.

x_1	y_1	x_2	y_2	x_3	y_3	x_4	y_4	U01	…	U12
0.5	1	1.5	1	0.5	-1	1.5	-1	0.0005943283904344		0.0005949147744104

Table 11. Numerical model configuration and parameters.

Item	Description
Geometry	2 *m* × 30 *m* rectangular plate
Material properties	Elastic modulus E = 22,000 *Pa*, Poisson's ratio ν = 0.33
Loading condition	Uniform tensile stress σ = 1 *MPa* applied on top and bottom edges
Crack configuration	Two horizontal edge cracks: Upper Crack: from (0.5, 1.0) to (1.5, 1.0) Lower Crack: from (0.5, -1.0) to (1.5, -1.0)
Number of unknown parameters	8 (4 crack-tip coordinates: $x_{1\text{-}4}$, $y_{1\text{-}4}$)
Parameter bounds	$x_1, x_2 \in [0.25, 1.75]$, $y_1, y_2 \in [0.75, 1.25]$ $x_2, x_4 \in [0.25, 1.75]$, $y_2, y_4 \in [-1.25, -0.75]$
FE mesh	6000 × 400 structured quadrilateral elements
Response points	12 points
OLHS sample size	500
Reference crack length a_0	1.0 *m*

Figures 9 and 10 show that, with the same training sample size, the RBF surrogate consistently outperforms Kriging. Its R^2 values stay near 1.0 and above the 0.99 acceptance level, while its RMSE remains below 0.01 and well under the 0.02 threshold, whereas Kriging fails to meet these accuracy criteria across all response points.

The comprehensive evaluation results from cross-validation of R^2 and RMSE demonstrate that the trained RBF surrogate model possesses excellent predictive accuracy and can be confidently used in the subsequent multi-crack inversion optimization process performed via MOPSO.

(4) Optimization Process and Results

The specific parameter settings of the MOPSO algorithm are shown in Table 12. Figures 11-14 illustrate the convergence history of the eight inversion parameters (crack tip coordinates x_1, y_1, x_2, y_2, x_3, y_3, x_4, y_4) during the MOPSO optimization process.

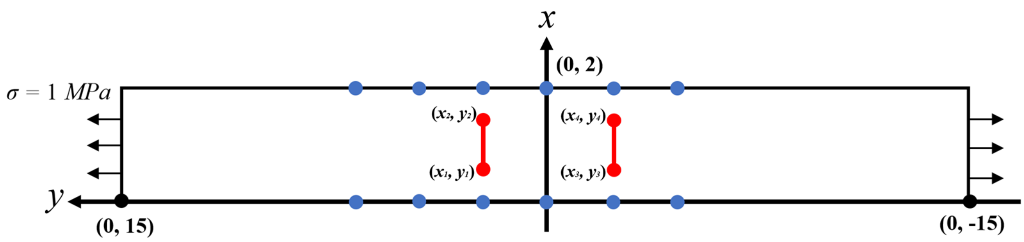

Fig. 8. Arrangement scheme.

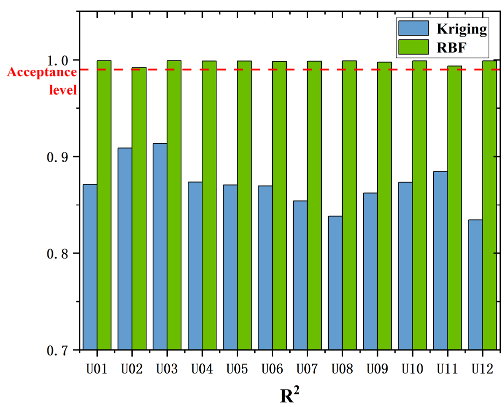

Fig. 9. Bar chart of R^2.

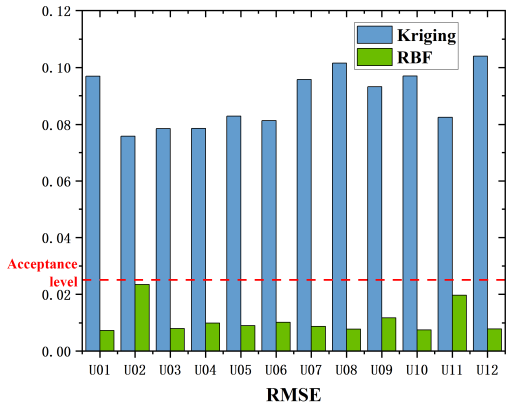

Fig. 10. Bar chart of RMSE.

Table 12. MOPSO parameter settings.

Parameter	Maximum Iterations	Swarm Size	Inertia Weight	Global Increment	Particle Increment	Maximum Velocity
Value	100	12	0.1	0.4	0.5	0.1

Table 13. Inversion results.

Crack coordinates	(x_{inv}, y_{inv})	(x_{true}, y_{true})	E_{pos}(%)
(x_1, y_1)	(0.50027, 1.018)	(0.5, 1)	1.80
(x_2, y_2)	(1.476, 1.0761)	(1.5, 1)	7.98
(x_3, y_3)	(0.49997, -0.9626)	(0.5, -1)	3.74
(x_4, y_4)	(1.5171, -1.0406)	(1.5, -1)	4.41

Table 14. Comparison of E_{pos} values obtained from different approaches.

Crack coordinates	$E_{KR+MOPSO}$(%)	$E_{KR+NSGA}$(%)	$E_{RBF+MOPSO}$(%)
(x_1, y_1)	10.12	22.54	1.80
(x_2, y_2)	15.59	20.97	7.98
(x_3, y_3)	4.65	12.81	3.74
(x_4, y_4)	5.91	23.64	4.41

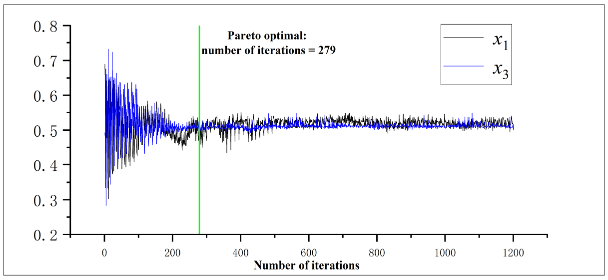

Fig. 11. Convergence history of x_1 and x_3.

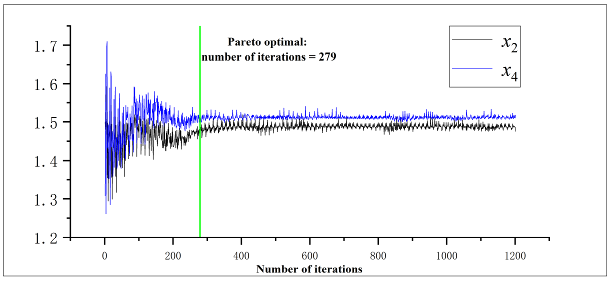

Fig. 12. Convergence history of x_2 and x_4.

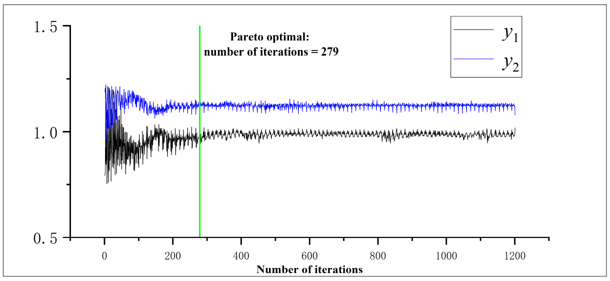

Fig. 13. Convergence history of y_1 and y_2.

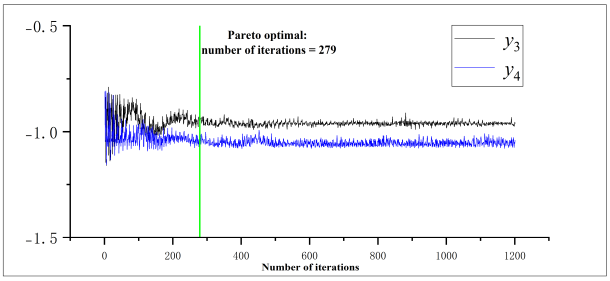

Fig. 14. Convergence history of y_3 and y_4.

As shown in Figs. 11- 14, the Pareto-optimal solutions were obtained at iteration 279. The inversion Results and error analysis is presented in Table 13. As in Section 3.1, the E_{pos} results obtained from different inversion methods are presented in Table 14.

As shown in Table 14, the RBF+MOPSO approach yields more accurate and stable predictions than the KR+MOPSO and KR+NSGA approaches under limited sample conditions.

3.3. Three parallel cracks under uniaxial tension

(1) Layout Scheme

A rectangular plate with dimensions of 2 m × 30 m is considered. The material has an elastic modulus of E = 22000 Pa and a Poisson's ratio of v = 0.33. Uniform tensile stress is applied to the upper and lower edges of the plate, identical to that in Section 3.2. The plate is assumed to contain three horizontally aligned, parallel internal cracks, each with a length of a = 1 m. The first crack is horizontally oriented, with its two crack-tip coordinates located at (0.5, 0) and (1.5, 0). The second and third cracks are also horizontally oriented, parallel to the first crack, and symmetrically arranged with respect to it. Their crack-tip coordinates are (0.5, -2.0) and (1.5, -2.0), and (0.5, 2.0) and (1.5, 2.0), as shown in Fig. 16. The plate is discretized using a structured mesh with n_H = 400 elements along the vertical direction, resulting in a total of 6000×400 elements. Each element is a four-node quadrilateral, allowing for an accurate representation of the geometry and boundary conditions.

(2) Surrogate Model Construction

The inverse parameter space consists of the coordinates of the six crack tips of the three horizontal cracks, totaling twelve parameters to be identified. Let the left and right crack-tip coordinates of the upper crack be (x_1, y_1) and (x_2, y_2), those of the middle crack be (x_3, y_3) and (x_4, y_4), and those of the lower crack be (x_5, y_5) and (x_6, y_6), respectively.

To generate the sample points required to train the RBF model using OLHS, the parameter ranges are defined as follows:

Upper crack: $x_1 \in [0.3,0.7]$, $y_1 \in [1.8, 2.2]$, $x_2 \in [1.3,1.7]$, $y_2 \in [1.8, 2.2]$

Middle crack: $x_3 \in [0.3,0.7]$, $y_3 \in [-0.2, 0.2]$, $x_4 \in [1.3,1.7]$, $y_4 \in [-0.2, 0.2]$

Lower crack: $x_5 \in [0.3,0.7]$, $y_5 \in [-1.8, -2.2]$, $x_6 \in [1.3,1.7]$, $y_6 \in [-1.8, -2.2]$

Subsequently, the OLHS method was applied within this twelve-dimensional parameter space to generate a total of 500 sample points for the XFEM computations. Twenty response points were used to extract displacement data. Their exact coordinates are listed in Table 15, and their locations on the plate are indicated by the blue markers in Fig. 16.

Table 15. Coordinates of response points for the double-crack model.

Axis	1	2	3	4	5	6	7	8	9	10	11	12	13	14	15	16	17	18	19	20
X	0	0	0	0	0	0	0	0	0	0	2	2	2	2	2	2	2	2	2	2
Y	-3	-2.5	-1.5	-1	-0.5	0.5	1	1.5	2.5	3	3	2.5	1.5	1	0.5	.5	-1	-1.5	-2.5	-3

Table 16. Sample data (Unit: meter).

Number	x_1	y_1	…	U01	…	U20
1	0.47395	1.83527		0.000548327		0.000548249
2	0.47956	1.85852		0.000549116		0.000549714
3	0.56132	2.07415		0.000549925		0.000549740
…						
500	0.49399	1.91142		0.000549302		0.000550054

Table 17. Target displacement data.

x_1	y_1	x_2	y_2	…	x_6	y_6	U01	…	U20
0.5	2	1.5	2		1.5	-2	0.0005497938254848		0.0005501307896338

Table 18. Numerical model configuration and parameters.

Item	Description
Geometry	2 *m* × 30 *m* rectangular plate
Material properties	Elastic modulus E = 22,000 *Pa*, Poisson's ratio ν = 0.33
Loading condition	Uniform tensile stress σ = 1 *MPa* applied on top and bottom edges
Crack configuration	Two horizontal edge cracks: Upper Crack: from (0.5, 2.0) to (1.5, 2.0) Middle Crack: from (0.5, 0.0) to (1.5, 0.0) Lower Crack: from (0.5, -2.0) to (1.5, -2.0)
Number of unknown parameters	12 (6 crack-tip coordinates: $x_{1\text{-}6}$, $y_{1\text{-}6}$)
Parameter bounds	$x_1, x_2 \in [0.3, 1.7]$, $y_1, y_2 \in [1.8, 2.2]$ $x_3, x_4 \in [0.3, 1.7]$, $y_2, y_4 \in [-0.2, 0.2]$ $x_3, x_4 \in [0.3, 1.7]$, $y_2, y_4 \in [-2.2, -1.8]$
FE mesh	6000 × 400 structured quadrilateral elements
Response points	20 points
OLHS sample size	500
Reference crack length a_0	1.0 m

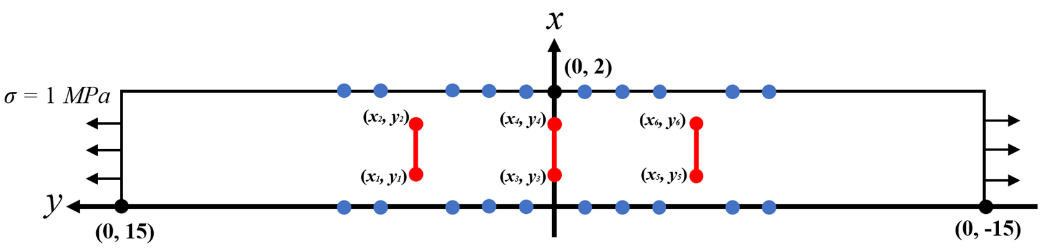

Fig. 16. Arrangement scheme.

Following the same procedures as in Sections 3.1 and 3.2, the sample data obtained from the XFEM calculations are presented in Table 16, and the target displacement values are listed in Table 17. Numerical model configuration and parameters are presented in Table 18.

(3) Accuracy Verification

Out of the total 500 sample points generated through OLHS and XFEM, 80 points were randomly selected for cross-validation analysis. The acceptable threshold for R^2 was set to 0.99, and for RMSE, to 0.02. The R^2 and RMSE values for the 20 response points (U01-U20), obtained through cross-validation, are presented in Figures 17 and 18 to compare the predictive accuracy of the RBF surrogate with the Kriging model using the same training-sample size.

Figures 17 and 18 show that, with the same training sample size, the RBF surrogate consistently outperforms Kriging. Its R^2 values stay near 1.0 and above the 0.99 acceptance level, while its RMSE remains below 0.01 and well under the 0.02 threshold, whereas Kriging fails to meet these accuracy criteria across all response points.

The comprehensive evaluation results from cross-validation of R^2 and RMSE demonstrate that the trained RBF surrogate model possesses excellent predictive accuracy and can be confidently used in the subsequent multi-crack inversion optimization process performed via MOPSO.

(4) Optimization Process and Results

The specific parameter settings of the MOPSO algorithm are shown in Table 19. Figures 19-23 illustrate the convergence history of the 12 parameters to be identified (crack tip coordinates x_1, y_1, x_2, y_2, x_3, y_3, x_4, y_4, x_5, y_5, x_6, y_6) during the MOPSO optimization process.

As shown in Figs. 19-23, the Pareto-optimal solutions were obtained at iteration 4687. The error analysis is presented in Table 20. As in Sections 3.1 and 3.2, the E_{pos} results obtained from different inversion approaches are presented in Table 21.

As shown in Table 21, the RBF+MOPSO approach yields more accurate and stable predictions than the KR+MOPSO and KR+NSGA approaches under limited sample conditions.

Table 19. MOPSO parameter settings.

Parameter	Maximum Iterations	Swarm Size	Inertia Weight	Global Increment	Particle Increment	Maximum Velocity
Value	100	50	0.1	0.3	0.5	0.1

Table 20. Inversion results.

Crack coordinates	(x_{inv}, y_{inv})	(x_{true}, y_{true})	E_{pos}(%)
(x_1, y_1)	(0.4938, 1.946)	(0.5, 2)	5.44
(x_2, y_2)	(1.5628, 1.9876)	(1.5, 2)	6.40
(x_3, y_3)	(0.48622, -0.03048)	(0.5, 0)	3.35
(x_4, y_4)	(1.4753, -0.0075637)	(1.5, 0)	2.58
(x_5, y_5)	(0.5342, -1.9446)	(0.5, -2)	6.51
(x_6, y_6)	(1.486, -2.0592)	(1.5, -2)	6.08

Table 21. Comparison of E_{pos} values obtained from different approaches.

Crack coordinates	$E_{KR+MOPSO}$(%)	$E_{KR+NSGA}$(%)	$E_{RBF+MOPSO}$(%)
(x_1, y_1)	1.51	14.34	5.44
(x_2, y_2)	3.78	23.21	6.40
(x_3, y_3)	2.20	21.15	3.35
(x_4, y_4)	12.05	27.28	2.58
(x_5, y_5)	5.33	17.06	6.51
(x_6, y_6)	9.72	17.87	6.08

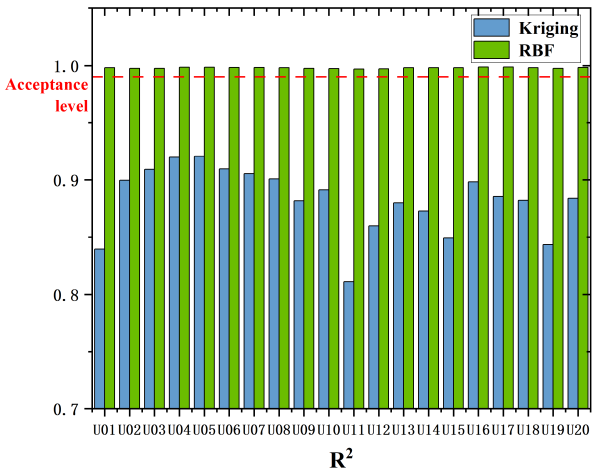

Fig. 17. Bar chart of R^2.

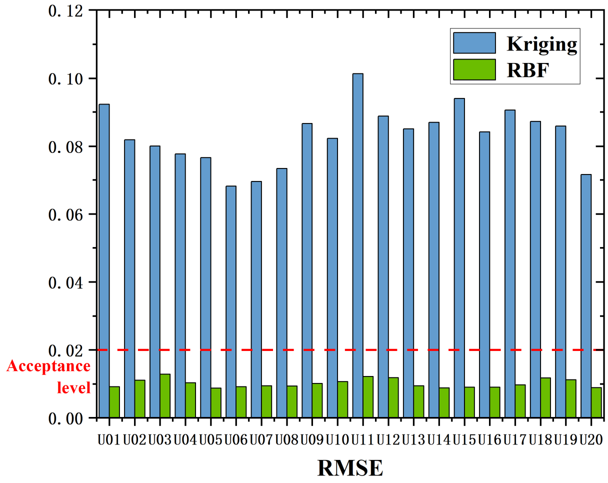

Fig. 18. Bar chart of RMSE.

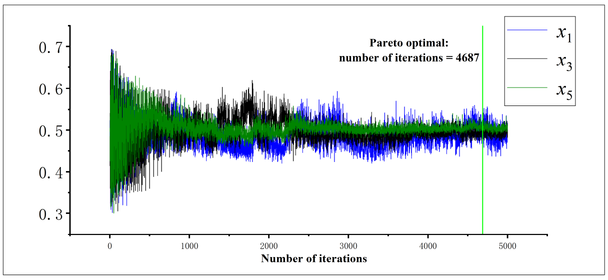

Fig. 19. Convergence history of x_1, x_3, and x_5.

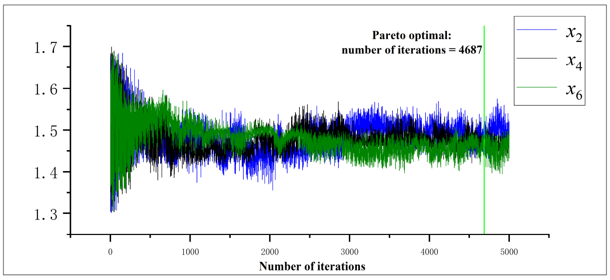

Fig. 20. Convergence history of x_2, x_4 and x_6.

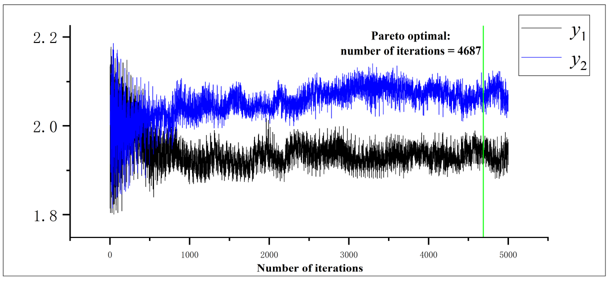

Fig. 21. Convergence history of y_1 and y_2.

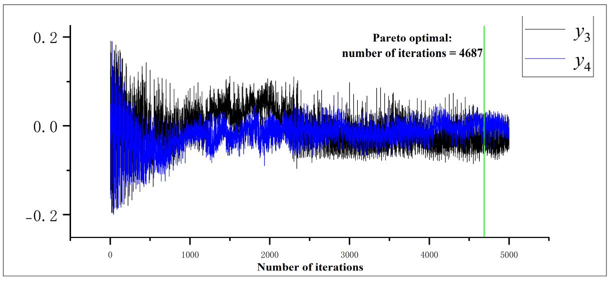

Fig. 22. Convergence history of y_3 and y_4.

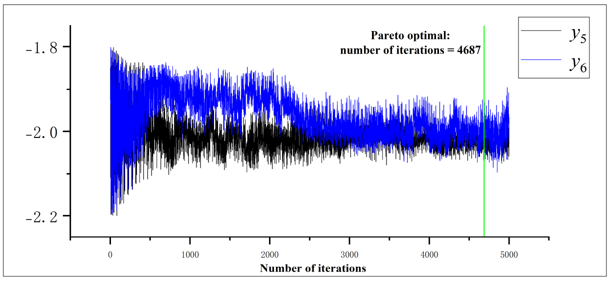

Fig. 23. Convergence history of y_5 and y_6.

4. Conclusion

The present study has developed a synergistic XFEM-RBF-MOPSO framework for efficient inversion of multiple interacting cracks with limited displacement measurements. The forward responses were generated through XFEM, while the RBF surrogate was trained to approximate the displacement field with high accuracy. MOPSO was employed to perform the inversion. Three numerical examples involving collinear double-edge cracks, two parallel internal cracks, and three parallel cracks were conducted to validate the proposed approach. The integrated XFEM-RBF-MOPSO framework demonstrates high predictive accuracy and computational efficiency, making it a promising tool for practical structural monitoring and multi-crack identification. It also provides an effective bridge between physics-based numerical modeling and data-driven inversion methods. The key findings of the present investigation can be summarized as follows:

1) The proposed XFEM-RBF-MOPSO method successfully identifies multiple crack-tip coordinates, with displacement-based positional errors below 8%.
2) The RBF surrogate model achieves R^2 values above 0.99 and RMSE values below 0.02, which are superior to those of the Kriging model under the same training-sample size. It also exhibits higher robustness and convergence stability.
3) Compared with the KR+MOPSO and KR+NSGA approaches, the proposed approach yields significantly lower crack-tip errors in multi-crack problems.

Author Contributions

G. Xie planned the scheme, initiated the project, and suggested the methods; Z. Zhou processed the data, wrote the manuscript, and created the figures; H. Li, H. Zhai, C. Wu, and S. Chen provided methodological ideas and site support. J. Liu, Y. Liu, and J. Zhou participated in the discussions. The manuscript was written through the contribution of all authors. All authors discussed the results, reviewed, and approved the final version of the manuscript.

Acknowledgments

Not applicable.

Conflict of Interest

The authors declared no potential conflicts of interest with respect to the research, author- ship, and/or publication of this article.

Funding

This work is supported by the National Natural Science Foundation of China (52475289), Major Science and Technology Projects of Henan Province (241100220300), and Key Scientific and Technological Project of Henan Province (252102221009, 242102221013 and 252102220092).

Data Availability Statements

The datasets generated and/or analyzed during the current study are available from the corresponding author on reasonable r equest.

Nomenclature

a	Crack length [m]	E	Elastic modulus [Pa]
U_k	The displacement of the k-th response point	x_n	The x-coordinate of the n-th response point
y_n	The y-coordinate of the n-th response point	σ	Applied stress [MPa]
ν	Poisson's ratio		

References

[1] Rabinovich, D., Givoli, D., Vigdergauz, S., XFEM-based crack detection scheme using a genetic algorithm, *International Journal for Numerical Methods in Engineering*, 71(9), 2007, 1051-1080.
[2] Rabinovich, D., Givoli, D., Vigdergauz, S., Crack identification by 'arrival time' using XFEM and a genetic algorithm, *International Journal for Numerical Methods in Engineering*, 77(3), 2009, 337-359.
[3] Zhang, C., Wang, C., Lahmer, T., He, P., Rabczuk, T., A dynamic XFEM formulation for crack identification, *International Journal of Mechanics and Materials in Design*, 12(4), 2016, 427-448.

[4] Khatir, S., Dekemele, K., Loccufier, M., Khatir, T., Wahab, M.A., Crack identification method in beam-like structures using changes in experimentally measured frequencies and Particle Swarm Optimization, *Comptes Rendus Mécanique*, 346(2), 2018, 110-120.
[5] Bouhala, L., Makradi, A., Belouettar, S., Younes, A., Natarajan, S., An XFEM/CZM based inverse method for identification of composite failure parameters, *Computers & Structures*, 153, 2015, 91-97.
[6] Agathos, K., Chatzi, E., Bordas, S.P., Multiple crack detection in 3D using a stable XFEM and global optimization, *Computational Mechanics*, 62(4), 2018, 835-852.
[7] Feerick, E.M., Liu, X.C., McGarry, P., Anisotropic mode-dependent damage of cortical bone using the extended finite element method (XFEM), *Journal of the Mechanical Behavior of Biomedical Materials*, 20, 2013, 77-89.
[8] Gao, W., Yuan, S., Ge, S., Gao, Y., Xie, Y., Inversion Identification of Cracks for Underground Shield Tunnel Structure Based on HHO-XFEM, *Journal of Computing in Civil Engineering*, 39(3), 2025, 04025015.
[9] Dai, M.J., Xie, M.Y., A novel inverse extended finite element method for structural health monitoring of cracked structures, *Ocean Engineering*, 325, 2025, 120786.
[10] Kubo, S., Sakagami, T., Ohji, K., Electric potential CT method based on BEM inverse analyses for measurement of three-dimensional cracks, *Computational Mechanics' 86: Theory and Applications*, Tokyo, 1986, 1323-1328.
[11] Noii, N., Khodadadian, A., Ulloa, J., Aldakheel, F., Wick, T., Francois, S., Wriggers, P., Bayesian inversion for unified ductile phase-field fracture, *Computational Mechanics*, 68(4), 2021, 943-980.
[12] Munawar, H.S., Hammad, A.W., Haddad, A., Soares, C.A.P., Waller, S.T., Image-based crack detection methods: A review, *Infrastructures*, 6(8), 2021, 115.
[13] Corrado, N., Durrande, N., Gherlone, M., Hensman, J., Mattone, M., Surace, C., Single and multiple crack localization in beam-like structures using a Gaussian process regression approach, *Journal of Vibration and Control*, 24(18), 2018, 4160-4175.
[14] Liu, Z., Ardabilian, M., Zine, A., Ichchou, M., Crack damage identification of a thick composite sandwich structure based on Gaussian Processes classification, *Composite Structures*, 255, 2021, 112825.
[15] Wang, H., Yuan, S., Xu, Q., Meng, Y., Ren, Y., A new GW-based heteroscedastic Gaussian process method for online crack evaluation, *Structural Health Monitoring*, 21(6), 2022, 2874-2889.
[16] Zhong, Y., Zeng, X., Hou, J., Wang, R., Wang, L., Zhao, D., Zheng, Y., A crack identification scheme based on neural network surrogate model and XFEM, *Physica Scripta*, 99(10), 2024, 106007.
[17] Gao, H.Y., Guo, X.L., Hu, X.F., Crack identification based on Kriging surrogate model, *Structural Engineering and Mechanics*, 41(1), 2012, 25-41.
[18] Gao, H., Guo, X., Ouyang, H., Han, F., Crack identification of cantilever plates based on a Kriging surrogate model, *Journal of Vibration and Acoustics*, 135(5), 2013, 051012.
[19] Wang, D., Hua, C., Dong, D., He, B., Lu, Z., Crack parameters identification based on a kriging surrogate model for operating rotors, *Shock and Vibration*, 2018(1), 2018, 9274526.
[20] Nabavi, S.M., Rekavandi, S.H., Analysis of stress intensity factors for functionally graded cylinders with multiple longitudinal cracks using finite element method, *Applied and Computational Mechanics*, 13(2), 2019, 125-136.
[21] Moës, N., Dolbow, J., Belytschko, T., A finite element method for crack growth without remeshing, *International Journal for Numerical Methods in Engineering*, 46(1), 1999, 131-150.
[22] Belytschko, T., Moës, N., Usui, S., et al., Arbitrary discontinuities in finite elements, *International Journal for Numerical Methods in Engineering*, 50(4), 2001, 993-1013.
[23] Feng, S.Z., Li, W., An accurate and efficient algorithm for the simulation of fatigue crack growth based on XFEM and combined approximations, *Applied Mathematical Modelling*, 55, 2018, 600-615.
[24] Bordas, S., Moran, B., Enriched finite elements and level sets for damage tolerance assessment of complex structures, *Engineering Fracture Mechanics*, 73(9), 2006, 1176-1201.
[25] Sutula, D., Kerfriden, P., van Dam, T., Bordas, S.P., Minimum energy multiple crack propagation. Part I: Theory and state of the art review, *Engineering Fracture Mechanics*, 191, 2018, 205-224.
[26] Benthem, J.P., Koiter, W.T., Asymptotic approximations to crack problems, *In: Methods of analysis and solutions of crack problems: Recent Developments in Fracture Mechanics Theory and Methods of Solving Crack Problems*, Dordrecht: Springer Netherlands, 1973, 131-178.
[27] Knowles, J.K., Sternberg, E., An asymptotic finite-deformation analysis of the elastostatic field near the tip of a crack, *Journal of Elasticity*, 3(2), 1973, 67-107.
[28] Budyn, E., Zi, G., Moës, N., Belytschko, T., A method for multiple crack growth in brittle materials without remeshing, *International Journal for Numerical Methods in Engineering*, 61(10), 2004, 1741-1770.
[29] Xie, G., Li, J., Li, H., Wang, L., Li, X., Geng, H., Crack growth evaluation based on the extended finite element and particle filter combined method, *Engineering Analysis with Boundary Elements*, 169, 2024, 106004.
[30] Stolarska, M., Chopp, D.L., Moës, N., Belytschko, T., Modelling crack growth by level sets in the extended finite element method, *International Journal for Numerical Methods in Engineering*, 51(8), 2001, 943-960.
[31] Ventura, G., Xu, J.X., Belytschko, T., A vector level set method and new discontinuity approximations for crack growth by EFG, *International Journal for Numerical Methods in Engineering*, 54(6), 2002, 923-944.
[32] Ventura, G., Budyn, E., Belytschko, T., Vector level sets for description of propagating cracks in finite elements, *International Journal for Numerical Methods in Engineering*, 58(10), 2003, 1571-1592.
[33] Sukumar, N., Chopp, D.L., Moës, N., Belytschko, T., Modeling holes and inclusions by level sets in the extended finite-element method, *Computer Methods in Applied Mechanics and Engineering*, 190(46-47), 2001, 6183-6200.
[34] Park, J., Sandberg, I.W., Universal approximation using radial-basis-function networks, *Neural Computation*, 3(2), 1991, 246-257.
[35] Lowe, D., Broomhead, D., Multivariable functional interpolation and adaptive networks, *Complex Systems*, 2(3), 1988, 321-355.
[36] Moody, J., Darken, C.J., Fast learning in networks of locally-tuned processing units, *Neural Computation*, 1(2), 1989, 281-294.
[37] Coello, C.C., Lechuga, M.S., MOPSO: A proposal for multiple objective particle swarm optimization, *In: Proceedings of the 2002 Congress on Evolutionary Computation (CEC'02)*, Vol. 2, IEEE, 2002.
[38] Tang, B., Orthogonal array-based Latin hypercubes, *Journal of the American Statistical Association*, 88(424), 1993, 1392-1397.
[39] McKay, M.D., Beckman, R.J., Conover, W.J., A comparison of three methods for selecting values of input variables in the analysis of output from a computer code, *Technometrics*, 42(1), 2000, 55-61.
[40] Feng, S.Z., Han, X., Ma, Z.J., Królczyk, G., Li, Z.X., Data-driven algorithm for real-time fatigue life prediction of structures with stochastic parameters, *Computer Methods in Applied Mechanics and Engineering*, 372, 2020, 113373.
[41] Xie, G., Zhao, C., Li, H., Du, W., Liu, J., Wang, Y., Wang, H., A combination of extended finite element method and the Kriging model based crack identification method, *Physica Scripta*, 98(11), 2023, 115109.
[42] Zhong, Y., Zeng, X., Wang, X., Xie, G., Hou, J., Li, Y., Xu, C., Crack identification approach integrating partition of unity XFEM and network-optimized fusion model, *Physica Scripta*, 100(7), 2025, 075214.

ORCID iD

Guizhong Xie https://orcid.org/0009-0008-7290-5884
Zhengyang Zhou https://orcid.org/0009-0008-1225-0986
Hao Li https://orcid.org/0000-0002-9528-6333
Hongfei Zhai https://orcid.org/0000-0001-9451-2880
Chao Wu https://orcid.org/0009-0007-1492-8159
Shenshen Chen https://orcid.org/0000-0003-2852-3893

Jun Liu https://orcid.org/0009-0004-9586-9602
Yang Liu https://orcid.org/0009-0006-3441-2945
Jie Zhou https://orcid.org/0009-0008-4114-9529

© 2026 Shahid Chamran University of Ahvaz, Ahvaz, Iran. This article is an open access article distributed under the terms and conditions of the Creative Commons Attribution-NonCommercial 4.0 International (CC BY-NC 4.0 license) (http://creativecommons.org/licenses/by-nc/4.0/).

How to cite this article: Xie G., et al., A Synergistic XFEM-RBF-MOPSO Based Approach for Multi-Crack Parameter Inversion, *J. Appl. Comput. Mech.*, xx(x), 2026, 1–14. https://doi.org/10.22055/jacm.2025.48636.5383

Publisher's Note Shahid Chamran University of Ahvaz remains neutral with regard to jurisdictional claims in published maps and institutional affiliations.